

Part III

INTRINSIC STRAIN LOCALIZATION

At room temperature, plastic deformation in bulk metallic glasses occurs highly localized in narrow shear bands. If sample dimensions reach the nanometer regime, however, deformation becomes more homogeneous and enhanced ductility is observed in recent experimental studies (see Section 1.3.3). Some people argue that this size dependent transition in deformation mechanisms could be connected to the intrinsic ductility of metallic glasses [62, 88]. According to them, catastrophic shear banding occurs only in the presence of surface flaws or other defects, which are more probable in larger samples causing the observed size effect.

To determine the intrinsic deformation mode of a metallic glass, we first investigate tensile deformation of a defect-free sample in the absence of free surfaces and compare the homogeneous nucleation of a shear band to the heterogeneous nucleation at a free surface. In the subsequent chapter, we investigate the size effect in metallic glasses by deforming nanowires with different diameters.

HOMOGENEOUS VS. HETEROGENEOUS SB NUCLEATION

It is generally assumed that homogeneous nucleation of shear bands would never occur in practice [61, 6], as the barriers to activate surface-STZs are significantly lower than for bulk-STZs [126]. Hence, shear bands would always form at a free surface before the theoretical yield stress is reached. This implies a shear band nucleation mechanism similar to dislocation nucleation, where the barriers for homogeneous nucleation are very high compared to nucleation at grain boundaries or surfaces, so it would hardly ever happen in practice [127]. In order to test this view, we investigate plastic deformation of homogeneous metallic glass in the absence of stress concentrators and free surfaces. Since we are interested in the deformation regime where shear banding is the dominant deformation mode, we have to choose the deformation conditions accordingly. Fig. 5 shows an example of an experimental deformation mechanism map where the operating deformation mechanism are given as a function of strain rate and temperature for an amorphous alloy. Unfortunately, the strain rate regime considered in this map, ranging from 10^{-6} to 10^4 s^{-1} , does not include the regime which is accessible with MD simulations. Due to the limited simulation time, deformation simulations are usually performed applying strain rates higher than 10^7 s^{-1} , which is orders of magnitude higher than typical experimental strain rates and experimental reference data in this regime are hardly available. On top of that, owing to the high cooling rates during glass preparation, computer samples are in a less relaxed state and more prone to thermal and mechanical activation than laboratory made samples. Taken these prerequisites, together with the uncertainty how the chosen interatomic potential reproduces metallic glass plasticity, there is a clear need to first map parameter space and determine the deformation regimes accessible with MD, before actually studying shear band nucleation in the presence and absence of free surfaces.

5.1 SIMULATION DETAILS

We simulated the uniaxial tensile deformation of a slab-shaped $\text{Cu}_{64}\text{Zr}_{36}$ glass sample, like the one shown in Fig. 8(b), with dimensions of $L_x \times L_y \times L_z = 37 \times 8 \times 75 \text{ nm}^3$ (1.3 million atoms) up to a strain of 20%. In order to compare the deformation

behavior with and without free surfaces, all simulations were performed using 3D-periodic boundary conditions (in the following labeled as '*3dp*'), as well as with open boundaries in *x*-direction (labeled as '*2dp*'). In the case of open boundaries, the surface was relaxed prior to deformation by energy minimization and the stress introduced by the free surfaces in *z*-direction was released. Tensile deformation was simulated as described in Section 2.1.3 by applying a constant strain rate in *z*-direction; the pressure normal to the loading direction was controlled to be zero to allow for lateral contraction. The temperature was controlled using a Berendsen thermostat [109]. A summary of all simulations discussed in this chapter is given in Table 2.

Table 2: Summary of simulation setups.

temperature	strain rate	boundaries
300 K	10^9 s^{-1}	2dp, 3dp
300 K	$4 \cdot 10^7 \text{ s}^{-1}$	2dp, 3dp
50 K	$1 \cdot 10^9 \text{ s}^{-1}$	2dp, 3dp
50 K	$1 \cdot 10^8 \text{ s}^{-1}$	2dp, 3dp
50 K	$4 \cdot 10^7 \text{ s}^{-1}$	2dp, 3dp

5.2 THE ROLE OF TEMPERATURE AND STRAIN RATE

Plastic deformation of crystalline metals is typically simulated at room temperature using strain rates in the range of $10^8 - 10^9 \text{ s}^{-1}$ (see e.g. [128]). We used this as a starting point and since short simulation times are preferable, we first evaluated the operating plastic deformation mechanisms at 300 K when a strain rate of 10^9 s^{-1} is applied. In Fig. 21, the distribution of local atomic shear strains is shown for snapshots of the deformed samples at an applied strain of 18%. The snapshots for the samples tested at 300 K with a strain rate of 10^9 s^{-1} reveal that plastic deformation is rather homogeneous for the *2dp*- as well as for the *3dp*-sample; strain localization in a dominant shear band does not occur. Instead, extended STZs are homogeneously distributed in the whole sample on different slip planes carrying plastic deformation. The stress-strain behavior is similar for both samples (see Fig. 22 (a) and (b), blue curves). In agreement with the observed deformation mechanisms, a sudden stress drop as typically found when shear band slip sets in, is missing. The maximum stress σ_{max} , which represents the onset of global yielding, as well as the corresponding strain $\epsilon(\sigma_{max})$ are independent of the boundary conditions. One possible explanation for the observed behavior is that in our computer sample the activation barriers for shear transformations are significantly lower than in a laboratory made glass due to the fast cooling rates

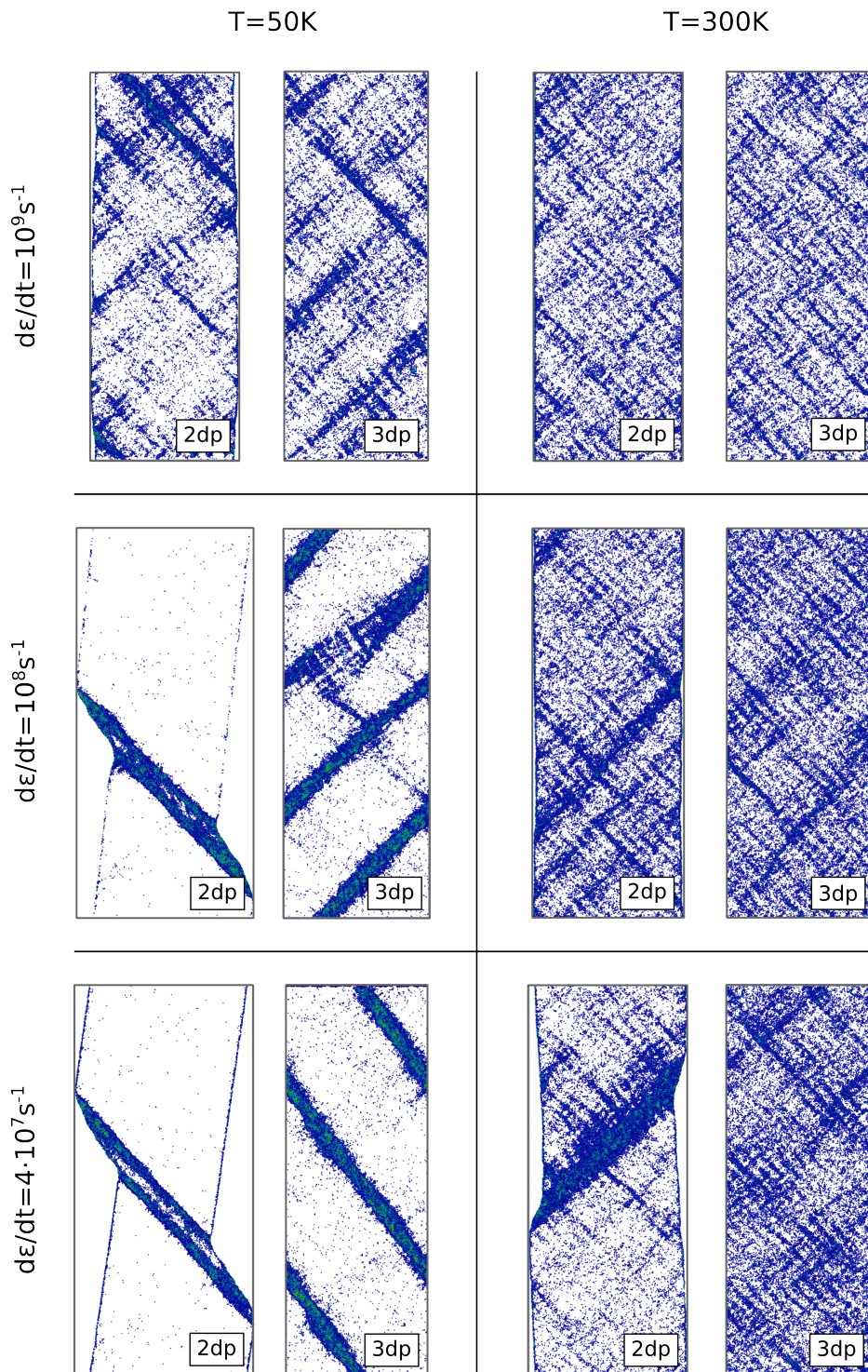


Figure 21: Snapshots of samples deformed in uniaxial tension at different temperatures and with different strain rates at $\epsilon = 18\%$. Only atoms with a local shear strain higher than 0.2, which indicate STZs, are displayed.

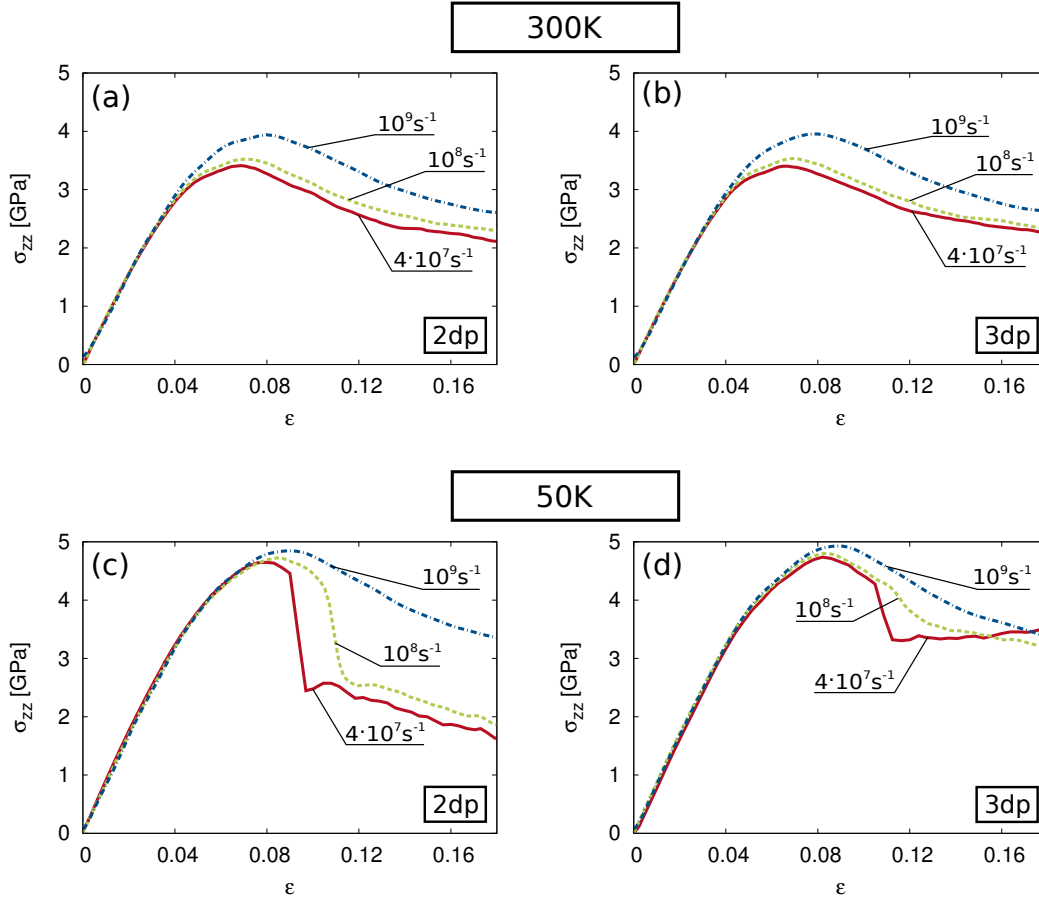


Figure 22: Influence of strain rate and temperature on the plastic deformation of a sample with free surfaces (a, c) and for a 3d-periodic sample (b, d). The samples were deformed at constant temperatures of 300 K (a, b) and 50 K (c, d).

for glass formation. Thermal activation at 300 K in addition to the high stresses introduced by the high strain rate leads to the activation of a large number of STZs in the whole sample and, hence, a homogeneous distribution of plastic strain. Consequently, a decrease in temperature should lead to more localized plastic deformation and represent more appropriate deformation conditions to study shear banding.

As expected, plasticity becomes more heterogeneous when the temperature is lowered to 50 K. Yet, the formation of an extended shear band is still not observed, neither for the periodic sample nor for the sample with free surfaces (see snapshots in Fig. 21). This behavior is attributed to the high deformation rate. According to Schuh *et al.* [51], homogeneous plasticity in metallic glasses does not only occur at high temperatures, but also at low temperatures and high

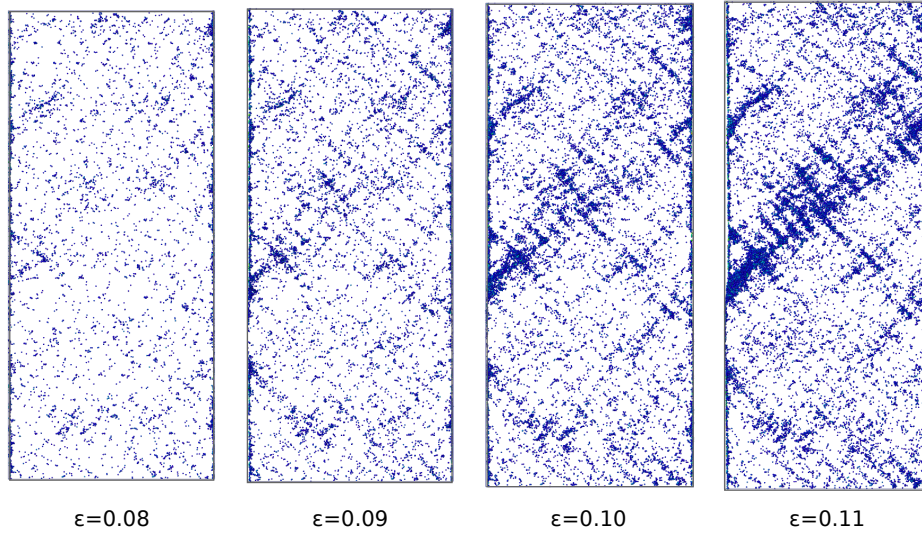


Figure 23: Snapshots of $2dp$ -sample at different strains during tensile deformation at 300 K with a strain rate of $4 \cdot 10^7 \text{ s}^{-1}$.

strain rates. If the applied strain rate is higher than the shear band nucleation rate, shear band nuclei cannot mature into extended defects and deformation becomes homogeneous. This is observable in the snapshots shown in Fig. 21, where a number of embryonic shear bands were formed by STZ percolation on different slip planes leading to an overall homogeneous distribution of plastic strain. Comparing the stress-strain curves for deformation with $\dot{\epsilon} = 10^9 \text{ s}^{-1}$ at 50 K and 300 K (Fig. 22, blue curves) we find that at 50 K the maximum stress is increased by approximately 1 GPa for both samples and that the maximum stress for the 3d-periodic sample is slightly higher as compared to the sample with free surfaces. The shape of the curves is similar for both samples and, again, no stress drop appears. Apparently, the shear band nucleation rate is lower than 10^9 s^{-1} and, thus, lower strain rates must be used for simulating shear banding.

We have, therefore, simulated room temperature ($=300 \text{ K}$) tensile deformation using a strain rate of 10^8 s^{-1} . The snapshots of the deformed samples in Fig. 21, however, show no significant differences in the deformation behavior as compared to the higher strain rate. Although the deformation appears slightly more localized, we still do not observe the formation of a dominant shear band, neither in the $3dp$ -sample nor in the $2dp$ -sample. The maximum stress is significantly decreased for both samples owing to the lower strain rate (see Fig. 22(a) and (b), green curves), but the principal shape of the stress strain curves resembles the curves for the higher strain rate.

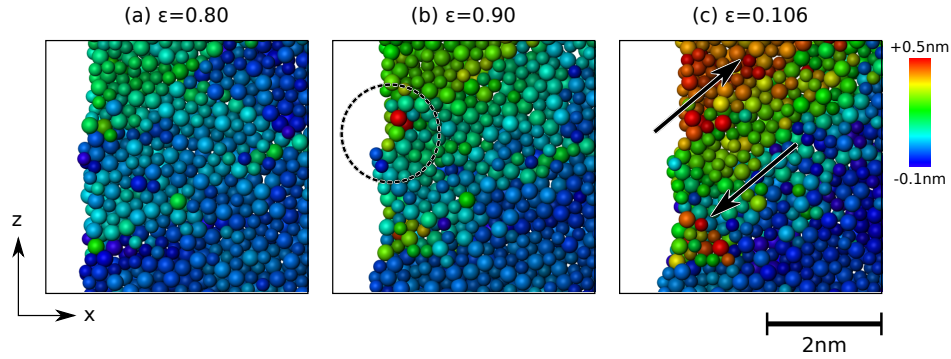


Figure 24: Shear band nucleation at a surface defect resulting from a STZ. The atoms are colored according to their displacement in x -direction.

Using an even lower strain rate of $4 \cdot 10^7 \text{ s}^{-1}$, which is close to the strain rate limit accessible with MD*, the sample with open surfaces forms one mature shear band. Looking at the snapshots in Fig. 21 we still observe extended STZs and embryonic SBs in the matrix facilitating a fraction of the applied strain. In the case of the $3dp$ -sample, the latter mechanism dominates and no mature SB occurs. The stress-strain behavior (Fig. 22(a) and (b), red curves) is almost identical for both samples and the maximum stress is further decreased due to the decrease in strain rate (compare Fig. 22(a) and (b), blue curves). But not only the σ_{max} , also the critical strain $\epsilon(\sigma_{max})$ is decreased owing to the extended time scales available for the activation of shear transformations. Interestingly, even though a shear band is formed in the presence of free surfaces, the stress strain behavior hardly deviates from the $3dp$ -case and no sudden stress drop occurs. In order to understand these observations, we have analyzed snapshots of the $2dp$ -sample at lower strain (Fig. 23) and, in fact, up to a strain of 10% plastic deformation is accommodated by extended STZs. STZs percolate along different slip planes and form SB nuclei, which are homogeneously distributed in the whole sample. At 10.6% strain, a shear band nucleates at the surface of the $2dp$ -sample and propagates towards the opposite surface. Subsequently, SB slip is the dominant plastic deformation mode. Looking at the displacements in x -direction at the SB-nucleation site (Fig. 24) reveals the processes which lead to SB formation: (a) at 8% the surface roughness is low and no surface defects are present that could serve as stress concentrators; (b) at 9% strain a STZ is activated at the surface and, since STZ operation involves the rearrangement of atoms in conjunction with volumetric changes, leaves behind a kink (as marked by circle); (c) in the following this kink serves as a stress concentrator and leads to shear localization

* Straining a system containing 1.3 million atoms to a strain of 20% using a strain rate of $4 \cdot 10^7 \text{ s}^{-1}$ requires to simulate a time of 5 ns, which means a computing time of typically 18 hours on 800 processors or 5-6 days on 128 processors.

(as indicated by arrows); the embryonic SB propagates through the sample and reaches the opposite surface at about 13% strain, when SB slip occurs. Given the results presented above, the formation of a shear band is not necessary to accommodate plastic strain if the samples are deformed at 300 K with a strain rate of $4 \cdot 10^7 \text{ s}^{-1}$. Thermal activation is sufficient to activate a large number STZs in the whole sample leading to an overall homogeneous deformation. The lower barriers for STZ activation at the surface become negligible due to the dominant effect of thermal activation, which leads to identical yield stresses for both samples. Yielding even occurs at the same strain as the density of potential STZs in the bulk is high resulting in similar nucleation rates with and without free surfaces. At the given deformation conditions, a SB forms only because a surface defect causes a local instability.

Finally, we simulated deformation at low temperature (50 K) and using low strain rates of 10^8 s^{-1} and $4 \cdot 10^7 \text{ s}^{-1}$. For the sample with free surfaces, plastic deformation occurs highly localized in one mature shear band (see snapshots in Fig. 21). In line with that, the stress-strain curves for deformation at low strain rates (Fig. 22 (c)) show a stress drop at the strain when SB slip sets in contrast to the curve for a deformation rate of 10^9 s^{-1} . The maximum stress is lower for lower strain rates, as well as $\epsilon(\sigma_{max})$ and the critical strain for SB slip.

In the absence of free surfaces, homogeneous nucleation of a shear band occurs when the sample is strained with a rate of 10^8 s^{-1} and $4 \cdot 10^7 \text{ s}^{-1}$ (see snapshots in Fig. 21). And while at the lowest strain rate the SB propagates on one defined slip plane, SB deflection at embryonic SBs on different slip planes and SB branching occurs for a strain rate of 10^8 s^{-1} . This result indicates that 10^8 s^{-1} is close to the SB nucleation rate leading to the formation of several SB nuclei. The stress-strain behavior supports this observation: for a strain rate of $4 \cdot 10^7 \text{ s}^{-1}$, the characteristic stress drop is present, while the stress release is much smoother when the sample is deformed with a strain rate of 10^8 s^{-1} .

While the operating deformation mechanisms will be discussed in more detail in the following chapter, we conclude that we have found simulation conditions which allow to simulate plastic deformation mechanisms observed in experiments. When a sample with free surfaces is deformed in tension at a temperature of 50 K, shear banding is the dominant deformation mechanism if the strain rate is 10^8 s^{-1} or lower. In the case of a 3d-periodic sample, on the other hand, a maximal strain rate of $4 \cdot 10^7 \text{ s}^{-1}$ should be used, due to the lower SB nucleation rate for homogeneous nucleation.

5.3 CHARACTERIZATION OF SB FORMATION MECHANISMS

As shown in the previous section, when a $\text{Cu}_{64}\text{Zr}_{36}$ glass sample is deformed in tension at 50 K using a strain rate of $4 \cdot 10^7 \text{ s}^{-1}$, plastic deformation occurs by the nucleation and propagation of one shear band, independent of the boundary

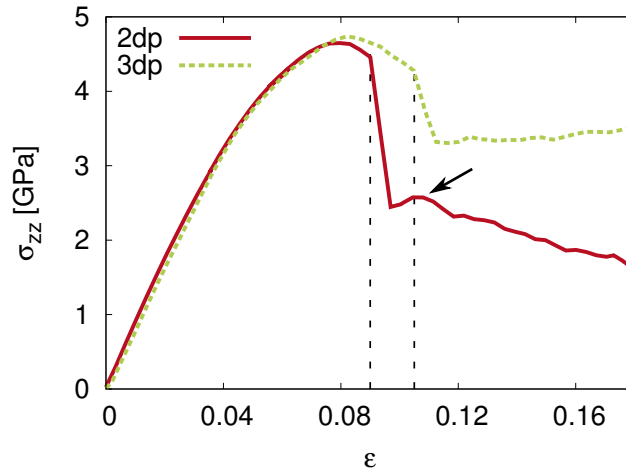


Figure 25: Stress-strain behavior of metallic glass samples deformed in uniaxial tension: comparison of a sample with free surfaces in one dimension (2dp) and a sample with the same dimensions, but 3d-periodic boundaries (3dp). Both samples deform by shear banding (onset marked by dashed lines).

conditions. The observation of dominant shear banding in a defect-free sample without free surfaces confirms that strain localization is an intrinsic metallic glass property and that extrinsic stress concentrators are not necessary. Looking at the stress-strain behavior of a sample with free surfaces and a fully periodic sample (Fig. 25), the curves look rather similar: the maximum stress for the 3dp-sample is 4.7 GPa, the maximum stress for the sample with free surfaces is only about 0.1 GPa lower. Only the critical strain for shear band formation (see dashed lines in Fig. 25) is about 0.015 lower in the presence of free surfaces. This behavior is surprising when thinking of SB nucleation mechanisms proposed in earlier work, where, as mentioned above, a lower activation barrier for surface shear transformations leads to SB nucleation at the surface at a stress well below the theoretical strength. If this assumption was true, the stress to nucleate a shear band in a fully periodic structure without free surfaces should be significantly higher, namely equal to the theoretical strength.

In order to explain our observations, we have calculated the local atomic shear strain and monitored atoms with a shear strain higher than 0.2 during deformation, which indicate shear transformations [32]. Snapshots of the sample with free surfaces during shear band nucleation as shown in Fig. 26 (a) show that an agglomeration of STZs starts from the surfaces and leads to the formation of an embryonic shear band at 9.2% strain, which then propagates through the sample to the opposite surface. When the shear band has fully penetrated the sample, slip transfer occurs accompanied by a stress drop, as indicated by the dashed line in Fig. 25, and the slip steps at the surfaces continuously grow. Hence,

shear band nucleation in the presence of free surfaces occurs by a heterogeneous nucleation mechanism.

In the absence of preferential nucleation sites as free surfaces, we found SB formation to occur in a 4-step-process (see Fig. 26 (b)): (i) Shear transformations take place in the whole sample. A higher density of STZs is observed in the maximum stress planes, where a larger number of STZs can be activated due to the high shear stress and the catalytic effect of STZs favoring successive STZs in their neighborhood [129] (Fig. 26 (b), $\epsilon = 0.098$). (ii) When a critical stress is reached, coalescence of STZs occurs, resulting in more extended defect(s), namely shear band nuclei (Fig. 26 (b), $\epsilon = 0.106$). Once a nucleus with a radius larger than a critical radius is formed, this defect will grow, leading to a local stress release, which arrests smaller nuclei resulting in localized plastic deformation. (iii) With increasing strain, the nucleus grows along the plane with the least resistance, meaning a plane that is structurally softer. Hence, the nucleus will grow along a path with high STZ-density, which is the case along the maximum stress planes, and form a shear band (Fig. 26 (b), $\epsilon = 0.107$). (iv) If the nucleus reaches other defects, like free surfaces, interfaces, other shear bands (or itself in the case of periodic boundaries), instable localized slip occurs in the SB plane (Fig. 26 (b), $\epsilon = 0.110$) and a stress drop appears in the stress-strain curve (see dashed lines in Fig. 25). This mechanism resembles certain characteristics of ductile fracture, which involves similar processes (see, e.g., [130]): (i) void nucleation and growth, (ii) void coalescence and formation of micro-cracks, (iii) crack growth along structurally weaker paths and (iv) instable crack growth and fracture.

Despite the different boundary conditions, the mechanisms of shear band formation are rather similar. The only substantial difference is that in the one case a SB nucleus forms heterogeneously at the surface, while in the other case nucleation is homogeneous. Since the nucleation rate is higher for heterogeneous nucleation and the critical strain is determined by the nucleation rate, we find a higher critical strain for the *3dp*-sample. Considering the model for shear band nucleation kinetics introduced by Schuh and co-workers [51] and taking into account the results presented in the previous section, we can estimate the rates for homogeneous and heterogeneous shear band nucleation: According to Schuh *et al.*, at high strain rates a kinetic limitation for SB nucleation leads to the homogeneous distribution of strain. The transition from shear banding to this homogeneous deformation regime occurs when the applied strain rate is similar to the shear band nucleation rate. In the previous section we observed homogeneous deformation of the *2dp*-sample for a strain rate of 10^9 s^{-1} and dominant shear banding at a strain rate of 10^8 s^{-1} . Consequently, the rate for heterogeneous SB nucleation lies between 10^8 s^{-1} and 10^9 s^{-1} . In the case of the *3dp*-sample we found a mixed deformation mode at a strain rate of 10^8 s^{-1} and, therefore, assume a rate for homogeneous SB nucleation in the range of 10^8 s^{-1} .

The reason why the maximum stress is similar for both samples is related to the simulation conditions. At the applied strain rate we are in a regime close to

HOMOGENEOUS VS. HETEROGENEOUS SB NUCLEATION

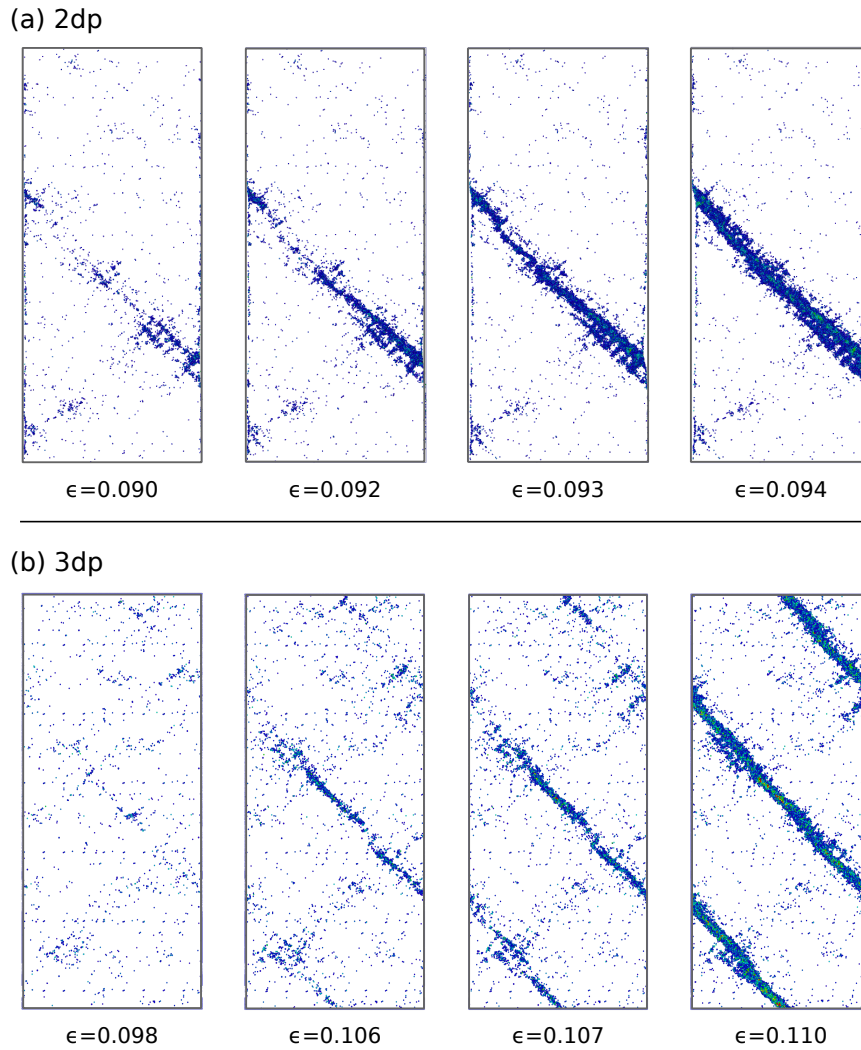


Figure 26: Shear band nucleation: snapshots of a sample with 2D-periodic boundaries (a-d) and the 3D-periodic boundaries (e-h) at different tensile strains; only atoms with a local shear strain higher than 0.2 which indicate shear transformations, are displayed.

the athermal limit, where thermal activation is almost negligible. Consequently, the critical stress for SB nucleation is close to the theoretical strength and almost independent of the presence of preferential nucleation sites at free surfaces.

After the large stress drop the stress-strain curves for the 2dp- and 3dp-sample (Fig. 25) exhibit different trends: while the stress slowly increases for the 3dp-sample, the stress acting on the 2dp-sample decreases after a small peak at about

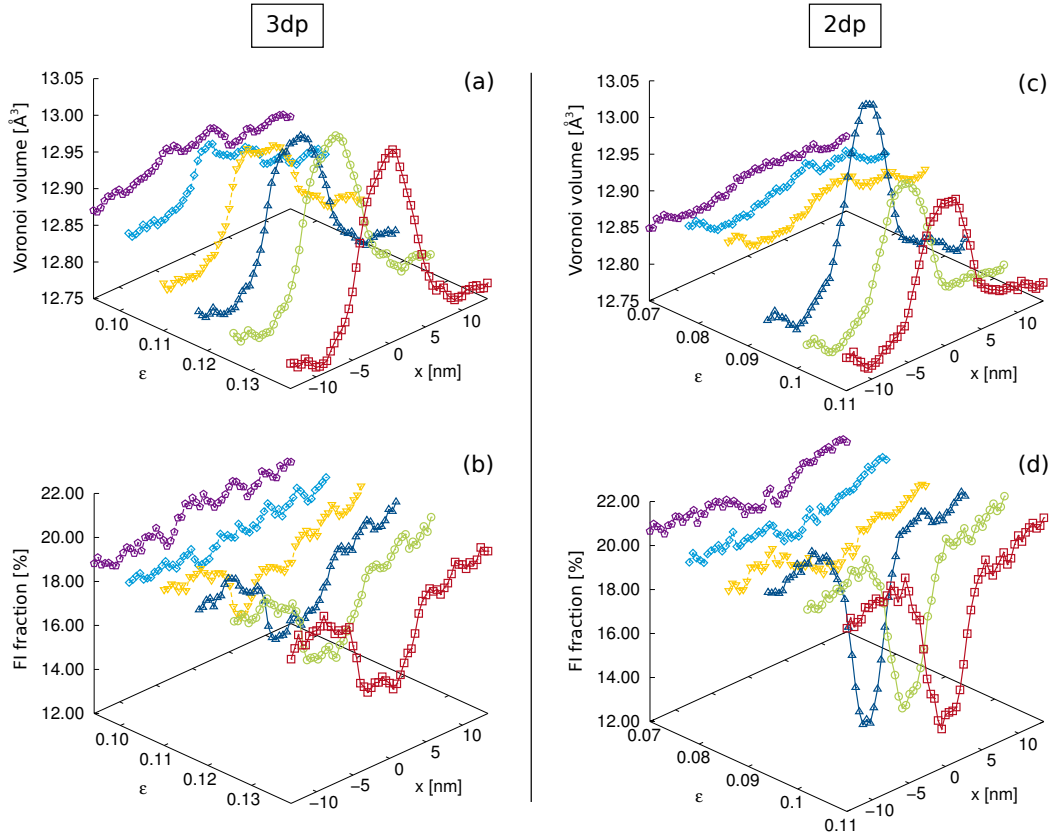


Figure 27: Scans of average Voronoi volume of Cu-atoms and FI-fraction over a shear band at $x = 0$ in (a-b) a sample with 3d-periodic boundary conditions and (c-d) a sample with free surfaces during tensile deformation.

10.5% strain. The reason for the stress increase in the case of the *3dp*-sample is that, due to the periodic boundary conditions, SB slip leads to the rotation of the slip plane away from 45° . Due to the less favorable Schmid factor, a higher external stress is required to keep up SB slip. In the presence of free surfaces, on the other hand, the stress decreases due to geometric softening, since the effective cross-section decreases. The small peak (marked by arrow in Fig. 25), which could indicate a strain hardening effect, cannot be explained at this point.

In order to get a better understanding of the atomic scale mechanisms involved in shear banding, we have analyzed the average Voronoi volume and short range order upon deformation. Particularly, the fraction of Cu-atoms coordinated in full icosahedra and their distribution in the sample were monitored. We have, therefore, scanned the average Voronoi volumes and the fraction FIs for snapshots at different strains during tensile deformation (see Fig. 27). The development of

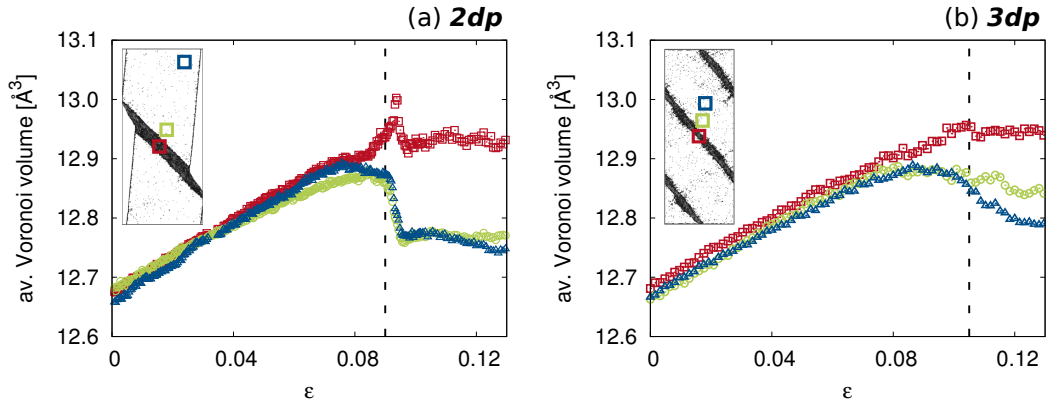


Figure 28: Local changes in Voronoi volume during deformation of (a) the $2dp$ -sample and (b) the $3dp$ -sample.

Cu- and Zr-Voronoi volumes during deformation is almost identical, thus only the results for the Cu-volumes are shown. For the case of the $3dp$ -sample (Fig. 27 (a) and (b)), up to a strain of about 9% the atomic volumes increase linearly and homogeneously in the whole sample, while the FI occupation decreases slowly in the whole sample from 22% in the virgin sample to 19.5%. At 9.4% strain, the scan of the FI-fraction shows a local decrease, which is accompanied by a local increase in the average Voronoi volume (see marked position in Fig. 27 (a) and (b)). This indicates the formation of an embryonic shear band, which subsequently grows to a width of 10 nm. From our results, the link between the destruction of FIs as a topological feature with high packing density and the creation of excess volume is obvious.[†] During SB slip, excess volume is generated which is seen as an increase of the Voronoi volumes inside the SB. At the same time, the Voronoi volumes in the undeformed matrix decrease as a result of a compressive stress component introduced by the volume expansion of the shear band. The topological short range order in the matrix is hardly affected since all deformation occurs localized inside the shear band, and the occupation of Cu-centered full icosahedra remains constant. In the unloaded sample, the Voronoi volumes in the SB are about 0.25 \AA^3 (or 2.0%) higher than in the matrix and the FI-fraction is 6% lower.

Similar characteristics are found for the case of the $2dp$ -sample with free surfaces in x -direction (Fig. 27 (c-d)). Yet, we observe one interesting difference: during shear band formation in the presence of free surfaces, the structural damage is more severe than in the $3dp$ -case and more free volume is created (see blue triangles in Fig. 27 (c-d)). When the SB subsequently slips, however, structural relaxations lead to a recovery of the extra-damage and the SB-structure

[†] We found that the average Voronoi volume of a Cu-atom in the center of a FI is 0.4 \AA^3 lower than the average volume of other Cu-atoms.

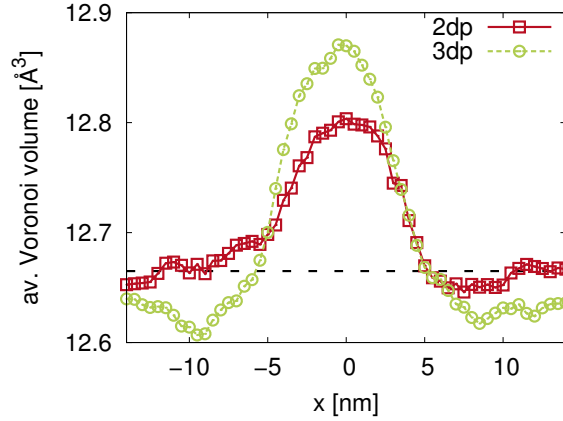


Figure 29: Scans of average Voronoi volume of Cu-atoms over a shear band at $x = 0$ for deformed and unloaded samples. The dashed line represents the average Cu-volume in the undeformed glass.

becomes comparable to the 3dp-case. This relaxation effect can also be seen in the corresponding snapshot in Fig. 21, where the structural recovery inside the SB is visible as a less strained region. Moreover, the structural relaxation could explain the aforementioned peak in the stress-strain curve at 10.5% (marked by arrow in Fig. 25), which indicates strain hardening.

In both samples we observed that the material surrounding a shear band is compressed when SB slip occurs. This compression, however, is not the result of a local redistribution of free volume. We monitored changes in average Voronoi volume in the 2dp- and 3dp-sample during deformation (Fig. 28) considering test volumes in the SB region (red), next to the SB (green) and at the largest possible distance from the SB (blue). If the observed densification was related to a local redistribution of free volume, we would expect a higher average Voronoi volume in the region away from the SB than in the region close to the SB. In agreement with the scans in Fig. 27, the analysis reveals that in both samples SB nucleation causes an increase in the Voronoi volumes inside the SB. In the 2dp-sample (Fig. 28 (a)), we even observe an overshooting when SB slip sets in. At the same time, the Voronoi volumes in the surrounding material decrease and so do the Voronoi volumes in the distant test volume. At the onset of SB slip (marked by dashed lines in Fig. 27), the sudden release of elastic strain leads to a distinct drop of the Voronoi volumes in the matrix for the case of the 2dp-sample. Again, the same behavior is found for both test volumes in the matrix. In the 3dp-sample, the decrease of the Voronoi volumes in the matrix is less pronounced due to the periodic boundary conditions constraining SB slip, which is in agreement with the only moderate stress drop observed in Fig. 25. Obviously, the contraction

of the matrix is caused by the release of elastic energy at the onset of SB slip, which enables the material outside the SB to relax into a more dense structural configuration. This effect is more pronounced in the case of the sample with open boundaries.

After unloading the samples at a tensile strain of 14%, scans of the average Voronoi volumes in the SB region (Fig. 29) reveal that in the presence of free surfaces, the matrix can release the compressive strain upon unloading and the average Voronoi volume in the matrix is similar to the undeformed state. In the case of the fully periodic sample, however, the matrix is still compressed after unloading.

5.4 SUMMARY

After exploring how the operating deformation mechanisms in a $\text{Cu}_{64}\text{Zr}_{36}$ glass are influenced by the applied strain rate and temperature, we determined simulation conditions which allow the simulation of shear banding with molecular dynamics. We observed shear banding in a defect-free sample without free surfaces and, therefore, confirmed that strain localization is an intrinsic metallic glass property, independent of the presence of extrinsic stress concentrators. Comparing homogeneous and heterogeneous SB nucleation we found that owing to the high strain rate, the critical stress is similar for both cases. The critical strain, however is lower in the presence of free surfaces which we attribute to the decreased SB nucleation rate for heterogeneous SB nucleation. The mechanisms for the formation of a SB nucleus are rather similar and involve the percolation of STZs along a viable shear path. Local shearing involves the destruction of densely packed icosahedral units leading to the generation of excess volume inside the SB. The sudden release of elastic energy at the onset of SB slip causes the contraction of the surrounding material, which is otherwise hardly affected by deformation. Interestingly, in the presence of free surfaces we observe structural relaxations inside the SB already during SB slip, which is observable also in the stress-strain response as a momentary stress increase.

STRAIN LOCALIZATION ON THE NANOSCALE

Recent experiments suggest a transition in deformation mode, from shear banding to a more homogeneous plastic deformation, if sample dimensions reach the nanometer regime [86, 87, 88, 89, 90]. Despite the growing number of reports on size-dependent plasticity, doubts about the intrinsic nature of this size-effect persist. When it comes to mechanical testing of nanoscale specimen, experimental artifacts due to tapering of cylindrical pillars for compression tests, surface modifications during sample preparation by focused ion beam, heating induced by the electron beam in *in-situ* mechanical testing, or confinement effects, can change the operating deformation mechanism. Moreover, size-independent deformation behavior and shear banding for sample-diameters as low as 150 nm was observed for various amorphous alloys [91, 92, 93]. Recent simulation results support the picture of size-independent shear banding until sample dimensions approach the SB thickness [94]. Only wires with poorly relaxed sample surfaces were found to deform by necking. Consequently, up to now the transition in deformation mode for nanoscale metallic glass samples is neither fully understood, nor is it absolutely certain that the observed size effect is an intrinsic metallic glass property. In this chapter, we present a systematic study on the deformation mechanisms of amorphous $\text{Cu}_{64}\text{Zr}_{36}$ nanowires under uniaxial tensile deformation.

6.1 SIMULATION DETAILS

We consider cylindrical samples with diameters of 5, 10 and 20 nm and an aspect ratio (height/diameter) of 2.5; the samples were periodic along the cylinder-axis and open boundaries were chosen laterally. Since it was reported that the relaxation of nanowire surfaces affects the operating deformation mechanism [94], we prepared wires in two different relaxation states: One set of wires was relaxed while the length of the cylinders was kept fixed ($\epsilon_{zz}^0 = 0$). After energy minimization, the wires were subsequently allowed to adjust their radial dimensions in 200 ps at 50 K. Because of the fixed length, the relaxed wires are not stress-free along the cylinder axis due to the surface stress. By deforming these samples we can model the simulation conditions in *in situ* tensile straining experiments of nano-samples which are not free standing, like in [88]. For the

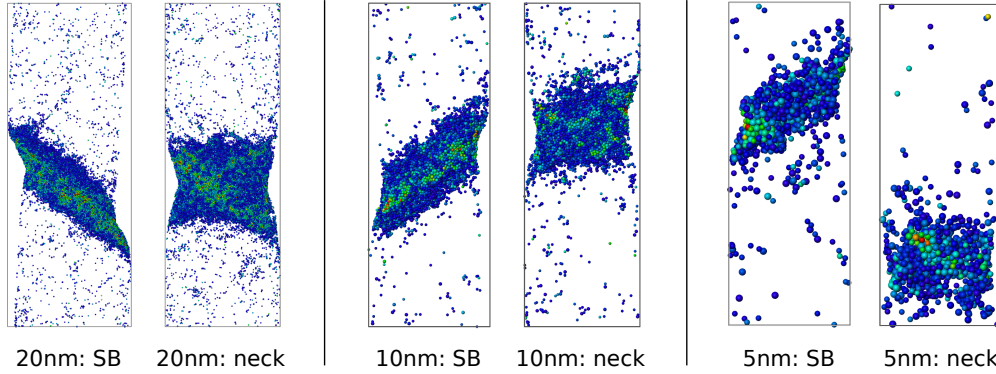


Figure 30: (a-f) Snapshots of deformed nanowires at $\epsilon = 12\%$ which deform by shear banding or by necking. Only atoms with a local atomic shear strain $\eta^{Mises} > 0.2$ are displayed; the atoms are colored according to η^{Mises} (blue: $\eta = 0.2$, red: $\eta = 0.6$).

other set of samples, the axial stress was subsequently released by relaxing the length of the cylinders to zero stress ($\sigma_{zz}^0 = 0$). The nanowires were all deformed in uniaxial tension along the cylinder axis by applying a constant strain rate of 10^8 s^{-1} at constant temperature; lateral contraction was facilitated by open boundaries. For each diameter we simulated 10 statistically independent tensile tests at 50 K. Additional tests were simulated at elevated temperatures of 300 K, 500 K, and 800 K ($\approx 0.85T_g$) for fully relaxed wires ($\sigma_{zz}^0 = 0$).

6.2 SIZE INDEPENDENT STRAIN LOCALIZATION

When deformed at low temperature (50 K), all nanowires exhibit strain localization, independent of the sample size. Even though the wires considered here are of smaller diameter than experimental samples which showed homogeneous plastic deformation, we did not observe significant uniform elongations. While most of the nanowires deform by shear banding, *i. e.*, strain localization in one dominant shear band, some wires deform by necking. Necking is a deformation mode typically found in ductile polycrystalline metals, but has also been observed experimentally in nanoscale metallic glasses [88, 90]. Both deformation modes occur for all sample sizes and relaxation states; typical examples of deformed nanowires are shown in Fig. 31(a). The high tendency for strain localization observed here is attributed to the fundamental processes governing plasticity in metallic glasses: At low temperature, shear transformation zones (STZs), which are stress-biased, thermally activated events, are strongly influenced by local stress and strain fields [48]. Therefore, STZs trigger subsequent STZs in the

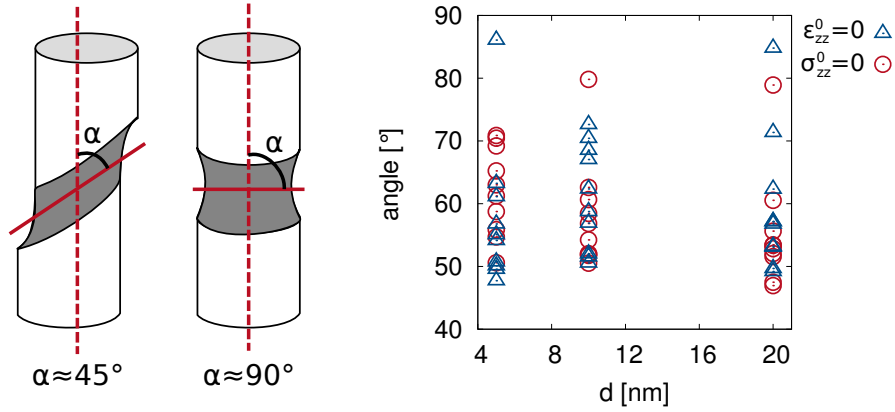


Figure 31: Average inclination angle of the deformation plane normal with respect to the deformation axis.

surrounding material, which finally leads to the autocatalytic assembly of STZs in extended flow defects like, e. g., shear bands.

For examining whether the occurrence of shear banding and necking is influenced by the diameter of the nanowires and their relaxation state, we determined the inclination angle between the deformation plane and the tensile axis. According to this criterion, a pure necking mechanism, where the deformation plane is perpendicular to the deformation axis, is characterized by an inclination angle of 90° . For a shear band we expect an inclination angle in the range of $50^\circ - 60^\circ$ [131]. The deformation plane normal was determined by fitting a plane to the atom positions located in the deformation zone (*i. e.*, shear band or neck), which we identified as atoms with a local atomic shear strain $\eta^{Mises} > 0.2$. If the size or relaxation state of the nanowires had an influence on the occurrence of shear banding or necking, respectively, this should be reflected in the inclination angles, as observed by Shi [94]. Shi reported an increase in the propensity for shear banding with increasing diameter, if wires had been prepared by simulated casting, while predominant necking was observed for samples cut from a bulk glass. These findings are in contrast to our results (Fig. 31(b)): Owing to the occurrence of both mechanisms, the inclination angles show a large scatter and we cannot detect a clear size effect. Moreover, we find no systematic influence of the initial relaxation state on the inclination angles. We attribute this discrepancy to the different interatomic potentials used: Shi simulated a binary Lennard-Jones (LJ) potential. Due to the mathematical format, the surface stress of a LJ system with a cutoff radius exceeding the first neighbor shell is necessarily negative, which causes the nanowires to swell [132, 133]. In our work, a modified Finnis-Sinclair type potential was applied, which simulates a positive surface stress, and causes the wires to shrink upon relaxation. In general, for the case of metallic materials

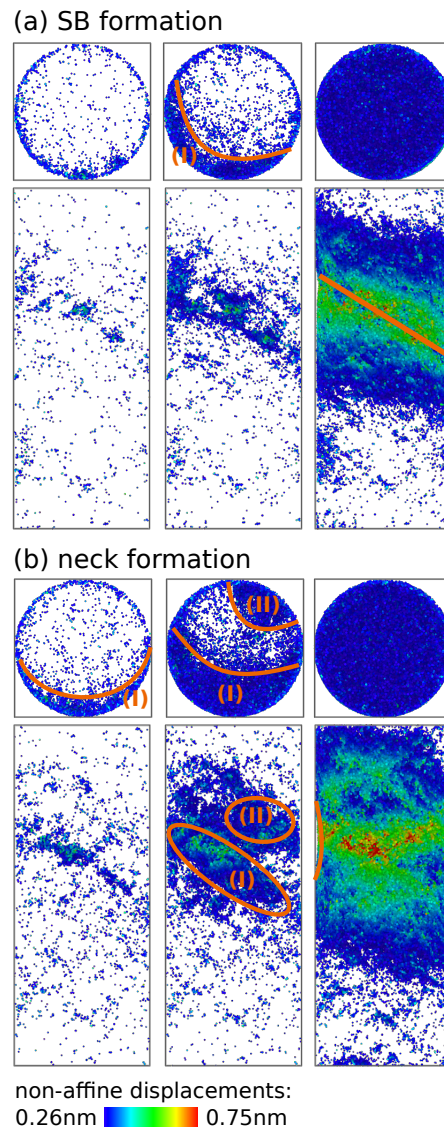


Figure 32: Snapshots of nanowires with $d = 20$ nm at the onset of strain localization in top and side view: (a) Formation of a single SB by nucleation from the surface at position (I); (b) formation of a neck by the coalescence of two SBs originating from the nuclei (I) and (II). Only atoms with a non-affine displacement larger than 0.26 nm, which corresponds to the Cu-Cu nearest neighbor distance in $\text{Cu}_{64}\text{Zr}_{36}$ glass, are displayed.

the surface stress is expected to be positive [134]. The results reported by Shi are, therefore, most likely a consequence of the LJ potential used for the simulations.

Next, we investigate the atomic scale processes involved in the formation of a shear band and a neck. We chose two nanowires with a diameter of 20 nm, one which deforms by shear banding and one which deforms by necking, and monitored the non-affine atomic displacements which indicate STZs. Fig. 32(a) illustrates the heterogeneous nucleation of a shear band at the surface: Due to the lower activation barrier for STZs at the surface, the number of displaced atoms at the surface is higher compared to the core of the wire. As discussed above, STZs have an autocatalytic effect leading to the formation of a SB nucleus, which then propagates through the nanowire along a maximum stress plane towards the opposite surface. When a neck forms, as shown in Fig. 32(b), the fundamental processes are similar: Again, we observe more STZs at the surface, where a SB nucleus forms by the percolation of neighboring STZs. Shortly after the first SB nucleus has formed, however, a second nucleus forms at the opposite surface on a different slip plane. Both embryonic SBs propagate towards each other and coalesce forming an extended deformation zone. Shear softening in this scenario is not limited to one narrow slip plane, but extends over a larger region in which the material yields by viscous flow.

6.3 THERMAL ACTIVATION

Whether the strain is localized in a SB or a neck is determined by the number of SB nuclei on different slip planes. At low temperatures, where the STZ activation rate is low due to low thermal activation, shear banding is the dominant deformation mechanism. If the temperature is increased and the STZ activation rate gets higher, we expect necking to occur more frequently, until finally homogeneous plastic flow prevails at temperatures close to the glass transition. We have simulated tensile tests at elevated temperature which actually support these assumptions (Fig. 33 (a-d)): While at 50 K deformation is highly localized in one narrow SB, at 300 K we already detect a higher STZ density in the matrix surrounding the dominant SB. If the temperature is further increased to 500 K, plastic deformation occurs by a necking mechanism, the neck being about 2-3 times the width of a SB; again, a high STZ density is observed in the matrix. Finally, at 800 K ($\approx 0.85T_g$) we observe homogeneous flow by the operation of individual STZs homogeneously distributed over the whole sample volume.

Applying the theory by Argon [50], the strain rate resulting from the activation and self-assembly of STZs in a metallic glass subjected to a stress τ can be expressed as

$$\dot{\gamma} = \alpha_0 \nu_0 \gamma_0 \cdot \exp\left(-\frac{\Delta F_0}{kT}\right) \sinh\left(\frac{\tau \gamma_0 \Omega_0}{kT}\right), \quad (6.1)$$

where α_0 is a constant of order unity which incorporates the volume fraction of material contributing to plastic flow, ν_0 is the attempt frequency of STZs, ΔF_0 is the activation free energy for STZs, γ_0 is the characteristic strain of a STZ

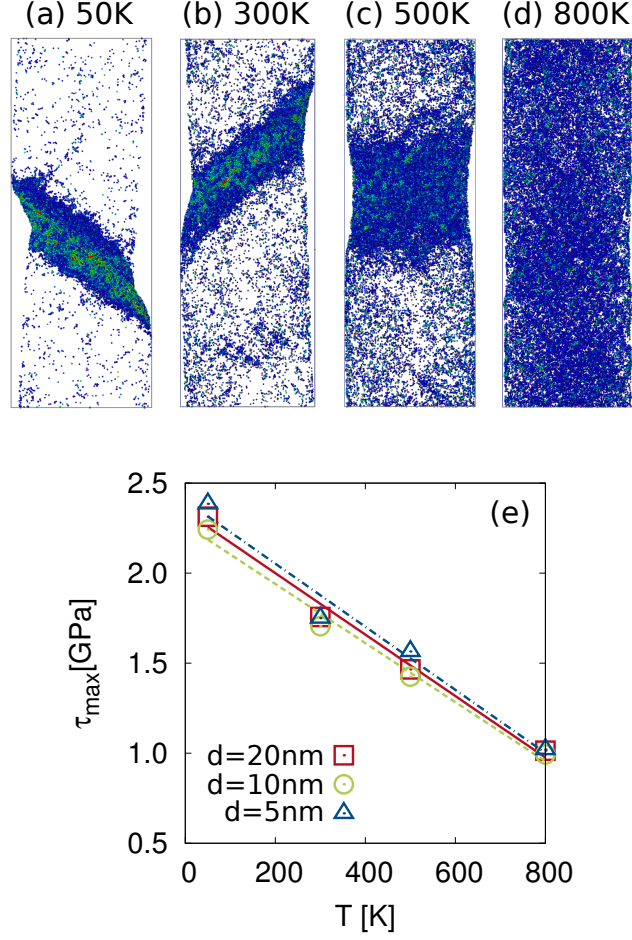


Figure 33: (a-d) Snapshots of nanowires with $d = 20\text{ nm}$ at a strain of 12% deformed at different temperatures. Only atoms with $\eta^{Mises} > 0.2$ are shown; color coding like in Fig. 31. (e) Maximum shear stress as a function of temperature for wires of different diameter and linear fits according to Eq.6.2.

(typically taken as 0.1), and Ω_0 is the characteristic volume of a STZ. Assuming $\tau\gamma_0\Omega_0/kT \gg 0$ and $\sinh(\tau\gamma_0\Omega_0/kT) \approx 0.5 \exp(\tau\gamma_0\Omega_0/kT)$, at a fixed strain rate we can rearrange Eq. 6.1 as [53]:

$$\tau = \frac{\Delta F_0}{\gamma_0\Omega_0} + \frac{kT}{\gamma_0\Omega_0} \ln \frac{2\dot{\gamma}}{\alpha_0\nu_0\gamma_0}. \quad (6.2)$$

In this form, we can directly compare the equation to our simulation results as shown in Fig. 33(e), where we plotted the maximum shear stress during tensile deformation at different temperature for wires of different diameter. By inserting $\gamma_0 = 0.1$ and $\alpha_0\nu_0 = 10^{11}\text{ s}^{-1}$ [51], we can calculate the characteristic volume of

a STZ from the slopes of each linear fit and obtain $\Omega_0 = 0.3 \text{ nm}^3$ (≈ 20 atoms), independent of the sample size. Using this value and the y-intercept in Fig. 33 the activation free energies ΔF_0 are determined to be 0.5 eV for all three sample sizes. In earlier studies (e. g., [50, 53, 51, 49, 56, 135]), STZs were found to contain between just a few up to 150 atoms which is in good agreement with the Ω_0 value extracted from our data. The activation free energy for STZs is slightly below the generally assumed range of 1-5 eV [4], which might be related to the high cooling rates during glass preparation in our simulations yielding a less relaxed atomic structure and, thus, lower barriers for STZs as compared to experiments.

6.4 SUMMARY

The observation of a size-independent activation free energy for STZ activation supports our assumption that there is no intrinsic size effect in metallic glasses which determines the operating deformation mechanism. Thus, the large homogeneous elongations observed in experimental studies of metallic glass nano-samples are either a strain-rate effect or promoted by extrinsic factors such as irradiation damage during FIB milling or heating in the electron beam during *in-situ* mechanical testing or confinement effects.

